Water Research 302 (2026) 126136

Contents lists available at ScienceDirect

Water Research

journal homepage: www.elsevier.com/locate/watres

Nanoconfinement-enhanced peroxymonosulfate activation by Co single atoms in hollow mesoporous carbon: Roles of active-site chemistry and mesoscale confinement

Hao Luo [a,1], Junli Zheng [b,1], Jiaxin Liu [a], Junjun Ma [a], Rui He [a], Chuqi Huang [a], Rong Xie [c], Qintie Lin [a,*]

[a] Guangdong Key Laboratory of Environmental Catalysis and Health Risk Control, Guangdong Industrial Contaminated Site Remediation Technology and Equipment Engineering Research Center, School of Environmental Science and Engineering, Guangdong University of Technology, Guangzhou 510006, China
[b] School of Environment and Civil Engineering, Dongguan University of Technology, Dongguan 523808, Guangdong, China
[c] School of Resources and Environment, Northeast Agricultural University, Haerbin 150030, Heilongjiang, China

HIGHLIGHTS

- A multiscale framework is developed to distinguish active-site chemistry from confinement-induced mesoscale effects in PMS activation.
- Nanoconfinement improves both pollutant degradation kinetics and PMS utilization efficiency.
- Singlet oxygen and electron-transfer processes jointly dominate nonradical oxidation in nanoconfined systems.
- Nanoconfinement enhances interfacial PMS activation on Co-N_4 sites by promoting adsorption and charge transfer.
- Catalytic enhancement in hollow mesoporous architectures is linked more to transport and microenvironment effects than to macroscopic curvature.

ARTICLE INFO

Keywords:
Peroxymonosulfate
Single-atom catalyst
Nanoconfinement effect
Hollow mesoporous carbon
Nonradical oxidation

ABSTRACT

Peroxymonosulfate (PMS)-based advanced oxidation processes have attracted considerable attention for the removal of refractory organic pollutants, yet their practical efficiency is still limited by the insufficient coupling between intrinsic active-site reactivity and interfacial mass transport. Here, the Co single-atom catalysts (Co-SACs) confined within hollow mesoporous carbon are constructed, and the effects of the nanoconfined environment on catalytic performance and reaction mechanism are systematically investigated. Compared with its unconfined counterpart, the nanoconfined catalyst exhibits accelerated pollutant degradation kinetics and improved PMS utilization efficiency (PUE). Combined quenching experiments, electrochemical analysis, and probe tests indicate that pollutant oxidation predominantly proceeds through a nonradical pathway involving singlet oxygen ($^1O_2$) and electron transfer process (ETP). Density functional theory calculations suggest that the confined structure strengthens PMS adsorption on the Co-N_4 sites and promotes interfacial charge transfer as well as the formation of the surface-bound PMS complexes (PMS*). COMSOL simulations further show that the mesoporous channels and hollow cavity could collectively enhance PMS activation by promoting reactant enrichment, accelerating fluid transport, and regulating the local microenvironment. From a multiscale perspective, this work elucidates how nanoconfinement influences PMS activation and suggests that the enhanced catalytic performance of hollow mesoporous architectures is more closely associated with confinement-induced mass-transfer regulation and microenvironment effects than with macroscopic curvature alone. This work provides mechanistic insight into PMS activation in nanoconfined Co-SACs systems and offers guidance for the rational design of highly efficient catalysts for nonradical oxidation processes.

---

* Corresponding author.
E-mail address: qintlin@163.com (Q. Lin).

[1] Co-first authors.

https://doi.org/10.1016/j.watres.2026.126136
Received 7 April 2026; Received in revised form 13 May 2026; Accepted 15 May 2026

1. Introduction

Peroxymonosulfate (PMS)-based Fenton-like advanced oxidation processes have attracted considerable attention owing to their strong oxidative capacity, broad operational pH range, and high efficiency for the removal of refractory organic contaminants (Zhao and Zhang, 2025). Compared with conventional homogeneous Fenton systems, heterogeneous PMS activation enables the generation of reactive species, mass-transfer behavior, and oxidation pathways to be regulated at the solid-liquid interface, thereby offering improved catalytic efficiency and stability (Guo et al., 2024). In this context, nanoconfinement has emerged as an effective strategy for enhancing PMS activation. Confined spaces can enrich reactants at catalytic interfaces, increase effective collision frequency, shorten diffusion distances, and modulate interfacial charge distribution as well as the local microenvironment, thereby influencing the formation and transformation of reactive intermediates (Dai et al., 2023; Fu et al., 2025; Terra et al., 2022). In particular, hollow structures, mesoporous channels, and hierarchically porous nanoreactors have often been associated with enhanced nonradical oxidation, such as singlet oxygen ($^1O_2$) generation and electron-transfer oxidation mediated by surface-bound PMS complexes (PMS*), resulting in improved degradation kinetics and oxidant utilization (Zhao et al., 2026). Despite these advances, the mechanistic origin of nanoconfinement remains insufficiently understood. The understanding of whether the enhancement is mainly attributable to the electronic modulation of active sites or to mesoscale effects, including local enrichment, accelerated transport, and microenvironment stabilization, is still far from clear.

Single-atom catalysts (SACs) have attracted extensive attention in Fenton-like oxidation systems because of their maximum atomic utilization, well-defined active centers, and tunable coordination environments (Zhu et al., 2025). Among various SACs, Co-based SACs (Co-SACs) are especially attractive because of their strong affinity toward PMS and high activation efficiency, which are beneficial for selective oxidation and efficient pollutant degradation (Xiao et al., 2023; Yin et al., 2023). Recent advances further suggest that integrating SACs with confined nanostructures is a promising strategy to boost catalytic performance beyond the intrinsic activity of isolated metal sites alone (Yin et al., 2023; Fang et al., 2024). For example, Xu et al. (Xu et al., 2023) developed a Co single-atom catalyst confined in N-doped hollow carbon spheres for PMS activation, showing that coupling Co-N_4 sites with a hollow carbon framework can markedly improve catalytic activity and durability. However, the role of confinement in that work was mainly associated with support effects and single-atom stabilization, rather than with an explicit mesoscale analysis of transport or microenvironment regulation. Notably, Meng et al. (Meng et al., 2024) exhibited that confining Co-SACs within mesoporous silica nanochannels enhanced local reactant enrichment and interfacial mass transport. More importantly, the confined environment alters the coordination environment and electronic structure of the Co sites, shifting the PMS activation pathway from a $^1O_2$-dominated route to a surface-mediated electron transfer process (ETP). This suggests that confinement in Co-SACs systems may play a role that extends beyond enhancing diffusion and adsorption to reshaping the electronic states of the active sites and redirecting the dominant reaction pathway. Nevertheless, most existing studies have focused primarily on the relationship between the local electronic structure of SACs and catalytic pathways (Mi et al., 2021; Zou et al., 2022), whereas the influence of surrounding spatial architecture on mass transport, reactant enrichment, and interfacial potential distribution remains insufficiently understood. As these factors are often intrinsically coupled in practical confined catalysts, their respective contributions to PMS activation are still difficult to distinguish.

Against this background, the widely discussed curvature effect in hollow structures deserves re-examination. Previous studies have frequently relied on highly curved carbon-based molecular models, such as small-radius nanotubes or strongly bent carbon frameworks, to represent the inner surfaces of hollow catalysts and to explain their superior catalytic performance. Based on these idealized geometries, the enhanced activity has often been attributed to curvature-induced modulation of adsorption energetics, orbital coupling, charge redistribution, and the electronic structure of active sites (Tang et al., 2024; Mao et al., 2026). While these studies have provided valuable insight into the possible local electronic effects of curved interfaces, caution is still required when directly extrapolating such interpretations to practical hollow architectures. Therefore, the beneficial effects of hollow architectures in practical catalytic systems may be more closely associated with confinement-induced mesoscale phenomena, such as reactant enrichment, transport regulation, residence-time extension, and interfacial potential redistribution, rather than with geometric curvature alone. To address this issue, the present work employs a multiscale strategy in which density functional theory is used to elucidate the intrinsic reaction steps and electronic responses of PMS activation at Co-SACs active sites, while COMSOL simulations are used to capture confinement-induced reactant enrichment, fluid transport, and concentration spatial distributions (Tian et al., 2025). This combined framework enables a scale-consistent evaluation of how hollow confined structures regulate PMS activation pathways and catalytic performance, and helps distinguish the respective roles of intrinsic active-site chemistry and mesoscale confinement effects.

Herein, Co-SACs supported on hollow mesoporous carbon were used as the model to decouple intrinsic SACs reactivity from confinement-induced mesoscale effects in PMS activation. By tailoring the cavity size and shell architecture, and integrating catalytic evaluation, oxidant utilization analysis, reactive-species probing, spectroscopy, theoretical calculations, and multiphysics simulations, we show that hollow nanoconfinement regulates PMS activation by enhancing mass transport, redistributing reactants, and modulating the interfacial microenvironment. On this basis, a multiscale framework bridging active-site chemistry and confinement-enhanced mesoscale regulation is established. This work provides a mechanistic basis for disentangling the respective roles of intrinsic active-site chemistry and confinement-induced mesoscale effects in PMS activation, and offers guidance for the rational design of high-performance nanoconfined Co-SACs for advanced oxidation processes.

2. Experimental section

2.1. Materials and chemicals

Details of the chemicals used in this study are provided in the Supporting Information SI (Text S1).

2.2. Synthesis of catalysts

The detailed synthesis procedures are provided in the Supporting Information (Text S2 and Figure S1), including the preparation of hollow mesoporous carbon sphere templates (Tian et al., 2024), deposition of the SACs-containing carbon layer, carbonization, and acid leaching with HCl.

Briefly, 38 mL of ethanol and 10 mL of deionized (DI) water were mixed at room temperature, followed by the addition of 5.0 mL of tetrapropoxysilane (TPOS). $CoCl_2 \cdot 6H_2O$ (0.03 g), 1,10-phenanthroline (0.10 g), and carbon spheres (60 mg, prepared as described in Text S3) were then added. The mixture was ultrasonicated for 20 min to achieve uniform dispersion and subsequently reacted at 60 °C for 6 h under reflux with stirring. The resulting solids were dried and calcined at 800 °C for 2 h under a N_2 atmosphere with a heating rate of 2 °C min^- (Zhao and Zhang, 2025). The calcined samples were then immersed in 1 M HCl for 24 h to remove residual Co clusters and unreacted Co species (Liu et al., 2022). After acid treatment, the samples were thoroughly washed with DI water until neutral pH and dried to obtain CoNC@HMCS$_{0.2}$, CoNC@HMCS$_{0.5}$, and CoNC@HCS. The former two samples possessed hollow mesoporous confined structures, whereas CoNC@HCS served as the unconfined control.

2.3. *Characterization*

Details of the catalyst characterization methods are provided in the Supporting Information (Text S3).

2.4. *Catalytic degradation experiments and analytical methods*

The catalytic degradation experiments for diclofenac sodium (DCF) and the related experimental procedures are described in Text S4. The degradation conditions for DCF and the corresponding kinetic equations are provided in Text S5. Detailed analytical methods are presented in Text S6, and the analytical procedures for the target contaminants are summarized in Table S1.

2.5. *Theoretical calculations*

Detailed methods for the DFT calculations and finite element simulations are provided in Texts S7 and S8, respectively.

3. Results and discussion

3.1. *Characterizations of catalysts*

In this study, two nanoconfined catalysts (CoNC@HMCS$_x$) and one unconfined catalyst (CoNC@HCS) were synthesized. While maintaining comparable chemical compositions among the three samples, pronounced differences in their three-dimensional architectures were deliberately engineered (Figure S1). Scanning electron microscopy (SEM) and transmission electron microscopy (TEM) analyses reveal that all samples exhibited spherical morphologies with narrow size distributions (Figs. 1a, 1b and Figure S2). Specifically, CoNC@HCS displayed a smooth surface and a hollow carbon-sphere structure with a shell thickness of ~6 nm. In contrast, CoNC@HMCS$_x$ featured a distinct hollow mesoporous framework with an average mesopore size of ~10 nm, and a substantially larger mean particle diameter (D ≈ 600 nm) than that of CoNC@HCS (D ≈ 300 nm), which lacked discernible pore channels. According to the cavity-to-sphere diameter ratios (r/R) of ~0.2 and ~0.5, the two CoNC@HMCS$_x$ samples were denoted as CoNC@HMCS$_{0.2}$ and CoNC@HMCS$_{0.5}$, respectively. Consistent with the TEM observations, Brunauer-Emmett-Teller (BET) measurements show that CoNC@HMCS$_{0.2}$ and CoNC@HMCS$_{0.5}$ possess high specific surface areas (SSAs) of 556 and 771 $m^2 \cdot g^{-1}$, respectively (Table S2). Their N_2 adsorption-desorption isotherms exhibit typical type-IV characteristics with pronounced hysteresis loops (Sing, 1989), and the corresponding pore-size distributions are centered at ~10 nm, confirming the mesoporous nature of the hollow frameworks (Figure S3). By comparison, CoNC@HCS exhibits a much lower SSA of 155 $m^2 \cdot g^{-1}$ and shows no evident mesoporous contribution in the pore-size distribution.

The surface of the carbon spheres together with the mesoporous channels provides abundant anchoring sites for stabilizing Co-SACs. The energy-dispersive X-ray spectroscopy (EDS) elemental mapping (Fig. 1c and Figure S4) reveals a homogeneous distribution of Co, N, and C throughout the carbon-sphere framework. Inductively coupled plasma (ICP) analysis further quantifies the low Co loadings, following the order of CoNC@HMCS$_{0.5}$ (0.27 wt%) > CoNC@HMCS$_{0.2}$ (0.25 wt%) > CoNC@HCS (0.24 wt%) (Table S3). Accordingly, the EDS signal of Co is noticeably weaker than that of the major elements. The discrete bright

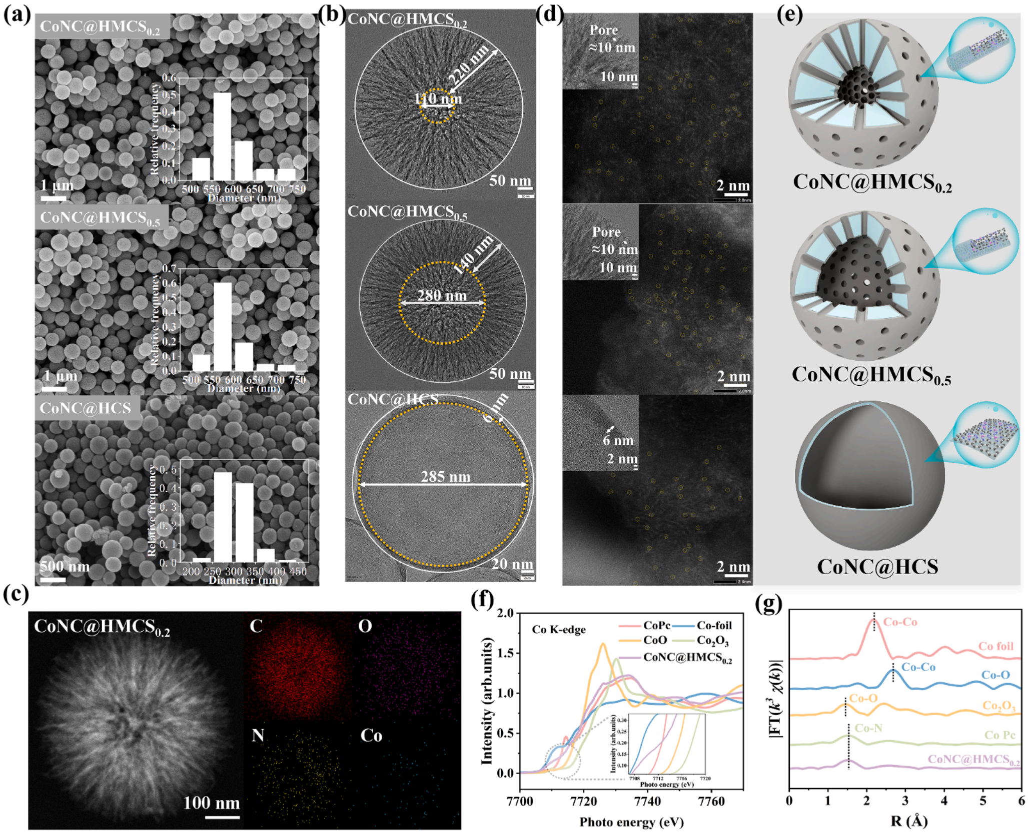

Fig. 1. SEM image and the particle size distribution (a); TEM images of the structure characteristics (b); EDS layered image of CoNC@HMCS$_{0.2}$ (c); TEM images of the mesoporous and AC—HAADF-STEM images of Co-SACs sites (highlighted by yellow circles) (d); Schematic diagram of the catalyst structures (e); Normalized Co K-edge XANES spectra of the Co-SACs and reference samples (CoPc, Co foil, CoO, and Co_2O_3) (f); Co K-edge FT-EXAFS spectra of the Co SACs and reference samples (CoPc, Co foil, CoO, and Co_2O_3) (g).

spots are clearly observed in the aberration-corrected high-angle annular dark-field scanning transmission electron microscopy (AC—HAADF-STEM) image (Fig. 1d), indicative of atomic-level dispersion of Co species. Meanwhile, X-ray diffraction (XRD) patterns show only the characteristic reflections of amorphous graphitic carbon at (002) and (100) for all catalysts (Figure S5) (Tang et al., 2024), with no detectable diffraction peaks attributable to Co-containing crystalline phases, further supporting the highly dispersed nature of the Co species.

X-ray photoelectron spectroscopy (XPS) measurements indicate that the three catalysts exhibit highly similar elemental compositions and valence-state features, suggesting similar surface chemical environments among the three catalysts (Figure S6). Considering that the low Co loading may lead to a limited signal-to-noise ratio and increase uncertainty in the deconvolution of Co-related XPS peaks, Co K-edge X-ray absorption spectroscopy (XAS) is further employed to elucidate the oxidation-state distribution and local coordination environment of Co species. The absorption edge position of CoNC@HMCS$_{0.2}$ lies between those of Co foil and CoO, suggesting that Co atoms are positively charged with an average oxidation state between 0 and +2 (You et al., 2025) (Fig. 1f). Moreover, the Fourier-transform k^3-weighted EXAFS spectrum of CoNC@HMCS$_{0.2}$ exhibits a pronounced peak at 1.4–1.6 Å, resembling that of CoPc and assignable to the first-shell Co-N coordination (Meng et al., 2024) (Fig. 1g). Quantitative EXAFS fitting yields a first-shell coordination number of 3.62 for Co-N, indicating that Co is predominantly present in a Co-N$_4$-like configuration (Figure S7 and Table S4). In the wavelet-transform (WT)-EXAFS contour map, CoNC@HMCS$_{0.2}$ shows the maximum intensity centered at ~5 Å^{-1}, further supporting atomically dispersed Co-N coordination (Figure S8). Collectively, these results demonstrate that the catalytically active sites consist primarily of isolated Co-SACs coordinated with N ligands and these Co sites in CoNC@HMCS$_x$ are located within a hollow mesoporous confined architecture, in sharp contrast to the relatively open, unconfined structure in CoNC@HCS (Fig. 1e).

3.2. *Catalytic degradation performance and reactive species identification during PMS activation*

In this work, DCF was selected as a representative contaminant to systematically evaluate the catalytic performance of the different catalysts. Notably, the nanoconfined CoNC@HMCS$_x$/PMS systems achieved complete DCF degradation within 8 min, with CoNC@HMCS$_{0.2}$/PMS exhibited a higher pseudo-first-order rate constant (k_{obs} = 1.2203 min^{-1}) than CoNC@HMCS$_{0.5}$/PMS (k_{obs} = 0.7690 min^{-1}). In contrast, the unconfined CoNC@HCS/PMS system showed substantially suppressed PMS activation, achieving only 47.3% DCF removal with a much lower k_{obs} of 0.0782 min^{-1}. These results indicate that nanoconfinement markedly enhances PMS activation, while tuning confinement-related structural parameters, such as cavity size, can further regulate the local reaction microenvironment and thereby influence catalytic performance. To clarify the origin of activity, Co-free HMCS$_{0.2}$ and NC@HMCS$_{0.2}$ were examined as control samples. Both controls showed poor PMS activation, resulting in only 11.8% and 25.4% DCF removal, respectively, indicating that Co sites serve as the primary active centers for PMS activation (Fig. 2a). In addition, single-factor control experiments demonstrated that adsorption and direct PMS oxidation contributed negligibly to DCF removal (Figure S9), excluding them as dominant pathways. Besides the accelerated degradation kinetics, the nanoconfined CoNC@HMCS$_x$ catalysts also exhibited markedly improved PMS utilization. The PMS utilization efficiency (PUE) was defined as the ratio of PMS equivalents consumed for contaminant mineralization to

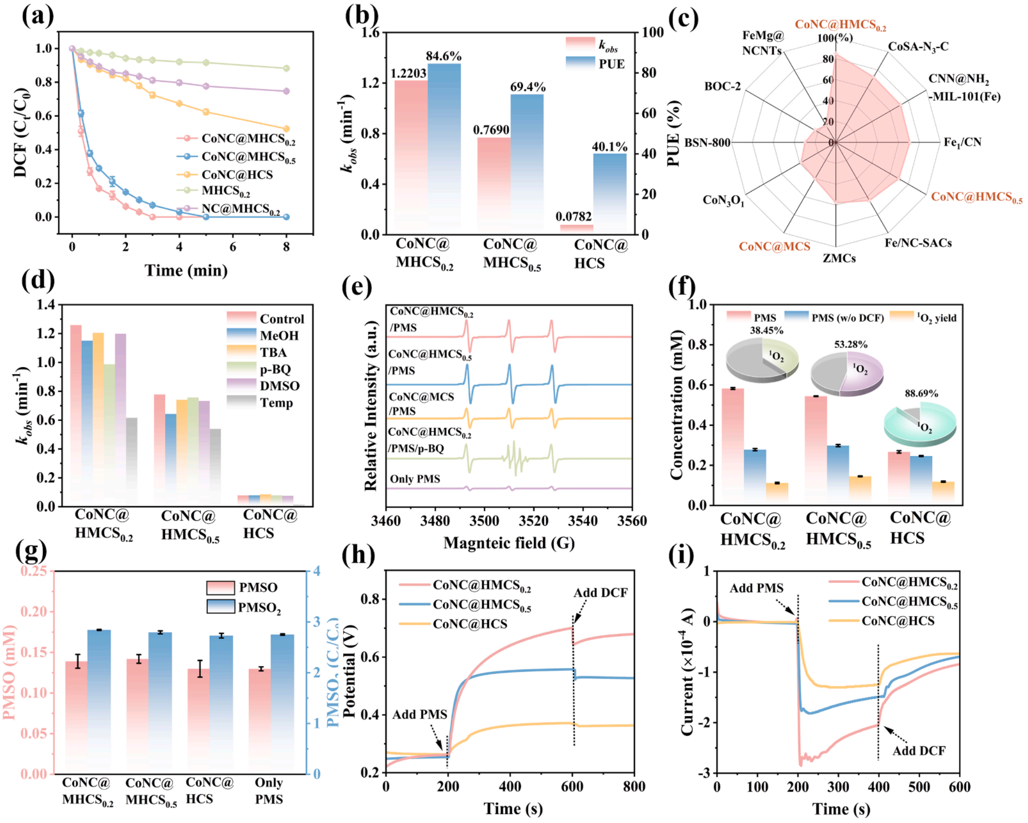

Fig. 2. Degradation rates of DCF with different reaction systems (a); corresponding k_{obs} and PUE of different catalyst/PMS systems (b); comparison with other reported catalysts in PUE for pollutant oxidation (c); effects of different scavengers on DCF degradation kinetics (d); EPR spectra obtained using TEMP as trapping agent (TEMP-$^1O_2$ = TEMPO) (e); the consumption of PMS and the relative content of $^1O_2$ (f); probe experiment of PMSO (g); open-circuit potentials (OCP) changes (h) and current-time (*i-t*) curves (i) upon sequential addition of PMS and DCF; Experimental conditions: [Catalysts] = 0.06 $g\cdot L^{-1}$, [PMS] = 1 mM, [DCF] = 20 mg·L^{-1} and initial pH = 6.75.

the total amount of PMS decomposed within the same time window (Text S9) (Wei et al., 2022), and was quantified based on TOC abatement (Figure S10) and PMS consumption (Figure S11). The CoNC@HCS/PMS system exhibited a low PUE of only 40.1%, whereas CoNC@HMCS$_{0.2}$/PMS and CoNC@HMCS$_{0.5}$/PMS achieved significantly higher values of 84.6% and 69.4%, respectively (Fig. 2b). These values are higher than those reported for many nonradical catalytic systems (Fig. 2c and Table S5). Collectively, these results demonstrate that nanoconfinement not only accelerates DCF degradation but also substantially improves oxidant utilization, highlighting the critical role of the hollow mesoporous confined architecture in regulating PMS activation efficiency.

Selective scavenger-quenching experiments were performed to systematically determine the identities of reactive oxygen species (ROS) produced during PMS activation over different catalysts. In the CoNC@HMCS$_{0.2}$/PMS system, the addition of methanol (MeOH; scavenger for $^{\bullet}$OH) (Wu et al., 2022), tert-butanol (TBA; scavenger for $SO_4^{\bullet-}$) (Wu et al., 2022), p-benzoquinone (p-BQ; scavenger for $O_2^{\bullet-}$) (Cai et al., 2024), or dimethyl sulfoxide (DMSO; scavenger for surface-bound radicals) (Wang et al., 2023) exerted negligible effects on DCF degradation. In contrast, inhibition of DCF degradation was observed only after the addition of 2,2,6,6-tetramethylpiperidine (TEMP; scavenger for $^1O_2$) (Gao et al., 2020). Notably, the inhibitory effect was relatively minor in the nanoconfined CoNC@HMCS$_x$/PMS systems but most pronounced in the unconfined CoNC@HCS/PMS system, indicating that $^1O_2$ participates in all systems, albeit with different relative contributions (Figure S12 and Fig. 2d). EPR spectroscopy using TEMP as a spin-trapping probe further verified substantial $^1O_2$ generation in all systems (Miao et al., 2021), and the time-normalized signal intensity of the TEMP-$^1O_2$ adduct followed the order: CoNC@HMCS$_{0.5}$/PMS > CoNC@HMCS$_{0.2}$/PMS > CoNC@HCS/PMS (Fig. 2e). Notably, p-BQ addition did not alter the TEMP-$^1O_2$ signal, suggesting that $^1O_2$ formation was not derived from $O_2^{\bullet-}$conversion. In parallel, no appreciable $O_2^{\bullet-}$ signal was detected, whereas only a weak $^{\bullet}$OH signal was observed, supporting a predominantly nonradical pathway (Figure S13) (Xu et al., 2023). Moreover, $^1O_2$ was quantified using 1,3-diphenylisobenzofuran (DPBF) as the chemical probe, and the ratio of $^1O_2$ production to PMS consumption was compared (Liu et al., 2020), yielding the order CoNC@HMCS$_{0.2}$ (38.45%) < CoNC@HMCS$_{0.5}$ (53.28%) < CoNC@HCS (88.69%) (Fig. 2f). Collectively, the scavenger tests, EPR results, and DPBF quantification indicate that nanoconfinement changes the relative contribution of $^1O_2$ during PMS activation and suggests the participation of additional nonradical pathways in the mesoporous-confined systems.

Beyond $^1O_2$, high-valent metal-oxo oxidation and ETP are also widely considered as potential nonradical pathways for PMS activation (Wang and Wang, 2020). First, methyl phenyl sulfoxide (PMSO) was employed as a diagnostic probe, yet no discernible signatures attributable to high-valent Co species (Co(IV)) were observed (Fig. 2g) (Zhou et al., 2021). This result argues against a dominant oxidative route dominated by additional formation of high-valent cobalt species under nanoconfinement. With respect to electronic conductivity and charge-transport properties, the three catalysts exhibited comparable Raman ID/IG ratios, indicating similar degrees of graphitization and only minor differences in the carbon framework (Zhao et al., 2017) (Figure S14). In contrast, electrochemical analyses revealed pronounced distinctions: CoNC@HMCS$_{0.2}$ displayed the highest specific capacitance and the lowest charge-transfer resistance, followed by CoNC@HMCS$_{0.5}$, as evidenced by cyclic voltammetry (CV) and electrochemical impedance spectroscopy (EIS) (Figure S15) (Zhou et al., 2021). These results suggest that the nanoconfinement architecture effectively enhances electron mobility and accelerates interfacial charge-transfer kinetics. Notably, PMS consumption by CoNC@HMCS$_{0.2}$ and CoNC@HMCS$_{0.5}$ exhibited a clear pollutant dependence, the PMS depletion behavior changed markedly in the presence of DCF. This observation suggests that an ETP pathway involving the PMS* may contribute non-negligibly to contaminant oxidation. Consistently, chronoamperometric (i-t) and open-circuit potential (OCP) measurements (Ren et al., 2020) showed rapid and significant current and potential responses upon addition of PMS and DCF for CoNC@HMCS$_{0.2}$ and CoNC@HMCS$_{0.5}$, whereas no comparable responses were detected for the unconfined CoNC@HCS (Figs. 2h and 2i). Moreover, the robust response maintained in the presence of $NaClO_4$ further supports the operation of a nonradical process under nanoconfinement (Figure S16) (Wang et al., 2021). These results collectively suggest that the hollow mesoporous confined architecture promotes local enrichment and interaction of PMS and pollutants, shortens the effective charge-transfer distance, and thereby favors short-range electron-transfer oxidation.

3.3. *DFT analysis*

Previous studies have suggested that nanoconfinement may promote oxidant activation and pollutant degradation by facilitating proton and charge transfer at confined interfaces (Li et al., 2025; Zuo et al., 2024). The accumulation and redistribution of protons and charges within confined spaces may also generate inner/outer interfacial potential differences, thereby altering local reactive environments and modulating reaction barriers and pathways (Yi et al., 2023; Tian et al., 2025). DFT calculations show that the PMS adsorption energy (E_{ads}) on the Co-N_4 configuration is −2.81 eV in the confined structure and −2.71 eV in the unconfined structure (Figure S17 and Fig. 3a), indicating stronger PMS binding in the confined model (Liu et al., 2023). Upon PMS adsorption, the CoNC@HMCS$_x$/PMS system exhibits an upward shift of the Co 3d-band center from −1.355 eV to −1.222 eV, toward the Fermi level, suggesting an enhanced propensity for interfacial charge transfer (Nørskov et al., 2011) (Fig. 3b). Compared with the unconfined CoNC@HCS/PMS model, the confined CoNC@HMCS$_x$/PMS model shows a more pronounced positive shift in the Co 3d-band center. In parallel, stronger orbital hybridization between Co 3d and PMS O 2p states is observed (Figs. 3b and c), accompanied by an additional 8.6% interfacial charge transfer (Fig. 3d), which favors PMS adsorption and facilitates the formation of PMS* (Zhang et al., 2023). These results support the view that confinement-enhanced interfacial electronic interactions promote PMS activation toward PMS* formation. This interpretation is also consistent with previous DFT studies based on Gibbs free-energy analyses (Meng et al., 2024; Wang et al., 2025), which suggested that strengthened PMS binding and an increased deprotonation barrier under nanoconfinement favor the conversion of PMS to PMS*, followed by pollutant oxidation via a mediated electron-transfer pathway (Fig. 3e).

3.4. *Modeling of confinement-induced mass transfer and microenvironment*

Previous studies investigating cavity curvature effects often employ DFT models with significantly curved carbon substrates to represent the ‘curved interface’ (Tang et al., 2024; Mao et al., 2026; Liang et al., 2025). However, it should be noted that the curvature radius in such models is typically at the nanometer or sub-nanometer scale, whereas the actual catalyst cavities often span tens to hundreds of nanometers, the local catalyst-reactant contact may differ substantially from such highly curved molecular-scale models. For sub-nanometer molecules such as PMS, the molecular size is far smaller than the cavity diameter, such that the actual reaction contact is confined to a limited local region of the inner surface. Therefore, directly extrapolating the ‘curvature-enhanced effect’ from highly curved models to sub-micrometer gap space (Li et al., 2023) may overestimate the contribution of cavity curvature to adsorption energy, orbital coupling, and charge transfer, and lacks clear geometric consistency (Wen et al., 2021). To address this, COMSOL used the actual structural features of the carbon spheres derived from electron microscopy as modeling parameters (Figure S18) (Tian et al., 2024), to simulate mesoscopic effects induced by cavity geometry, including local concentration enrichment, transport

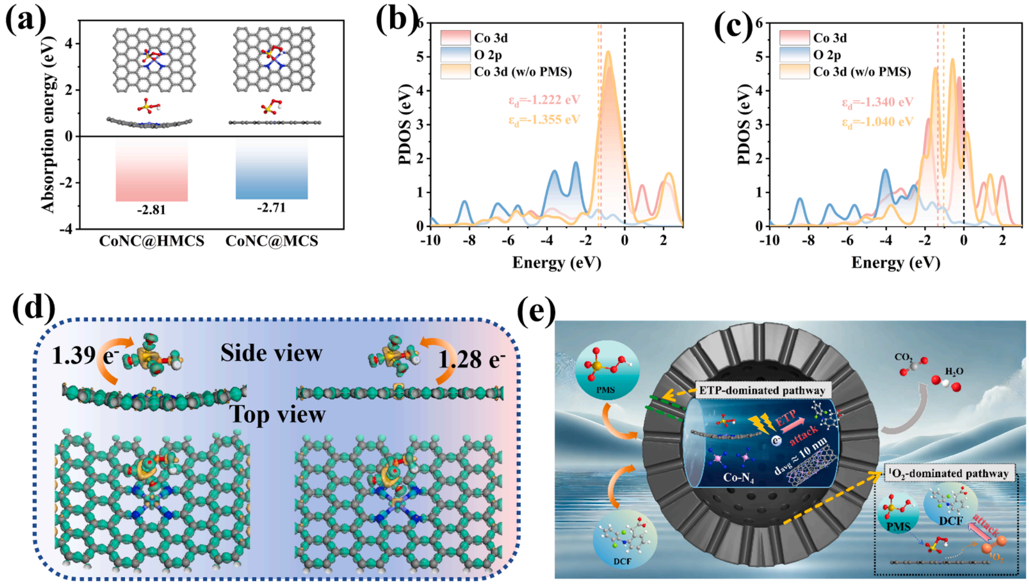

Fig. 3. The adsorption energy of PMS on CoNC@HMCS$_x$ and CoNC@HCS (a); PDOS of CoNC@HMCS$_x$/PMS (b) and CoNC@HCS/PMS (c); CDD map (yellow and green regions indicate electron accumulation and depletion, respectively) (d); the schematic illustration of the Fenton-like reaction for CoNC@HMCS$_x$ (e).

variation, and reduced diffusion distances.

Compared with the non-mesoporous hollow sphere (CoNC@HCS), the mesoporous hollow structure exhibits a pronounced pressure gradient between the external surface and the interior cavity (Fig. 4a and Figure S19). This pressure drop across the mesoporous channels indicates that the surrounding solution can be driven through the pores into the hollow interior, thereby establishing internal fluid pathways within the nanoreactor. Such transport substantially enhances the contact between the reactant solution and the catalyst surface, effectively increasing the accessible catalytic interface (Tian et al., 2023). Under this pressure-driven transport, a noticeable fluid acceleration occurs inside the mesoporous channels. To visualize the internal hydrodynamic behavior, a two-dimensional model based on the central cross-section ($y = 0$) was constructed for hollow spheres with different cavity ratios ($r/R = 0.2$ and 0.5, $R = 300$ nm) (Figure S20). The velocity mapping revealed that the mesoporous channels serve as high-velocity

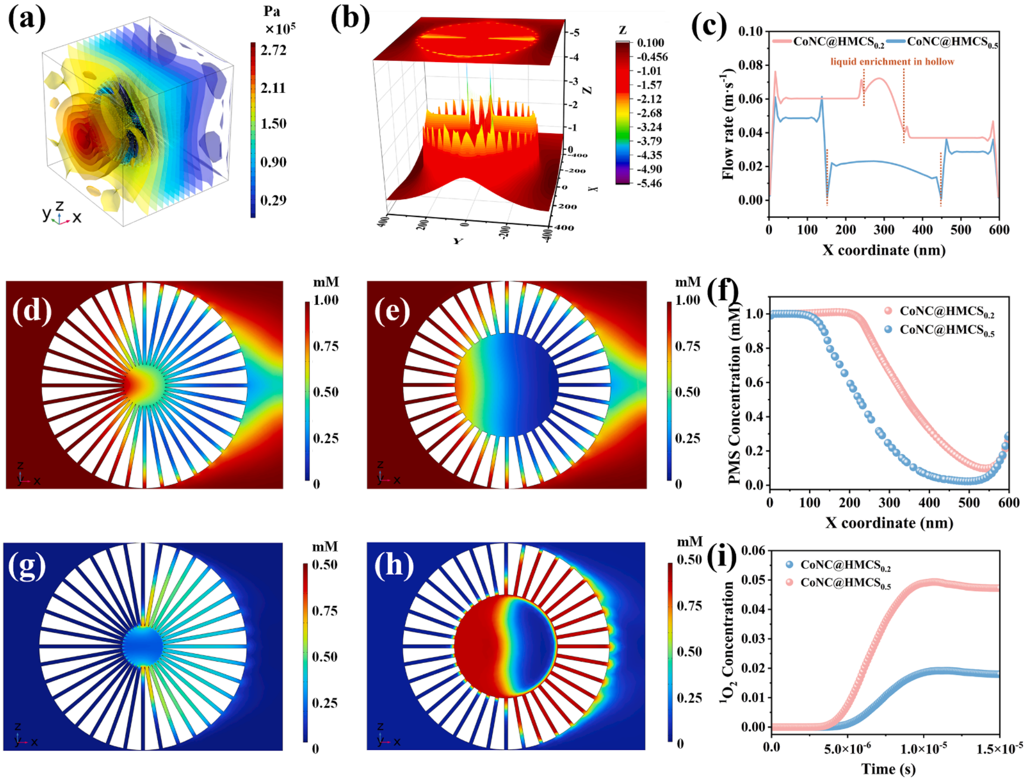

Fig. 4. Equivalent surface of pressure distribution in the fluid field with the sphere model (CoNC@HMCS$_{0.2}$) (a); 3D color mapping of the spatial flow velocity distribution on the cross-section (CoNC@HMCS$_{0.2}$) (b); Fluid velocity distribution across CoNC@HMCS$_{0.2}$ and CoNC@HMCS$_{0.5}$ (c); Spatial distribution of PMS concentration in the CoNC@HMCS$_{0.2}$ and CoNC@HMCS$_{0.5}$ (d-f); Spatial distribution of $^1O_2$ concentration in the CoNC@HMCS$_{0.2}$ and CoNC@HMCS$_{0.5}$ (g-i).

regions, while the hollow cavity maintains relatively slower flow (Fig. 4b). The elevated flow velocity in the channels facilitates the rapid transport of PMS molecules, resulting in a spatial distribution of PMS concentration that closely follows the flow field, with clear enrichment along the pore channels (Fig. 4b, Figures S21 and S22). Further numerical analysis reveals that cavity size significantly influences the internal hydrodynamics. In the smaller cavity model (r/R = 0.2), the flow velocity within the pores is higher and more uniform, indicating more efficient mass transfer and reduced transport resistance (Fig. 4c). Correspondingly, PMS molecules can reach the cavity center more rapidly, leading to a higher average PMS concentration within the hollow region (Figs. 4d-f). In contrast, the larger cavity (r/R = 0.5) exhibits a stronger velocity gradient between the pores and the cavity interior, which slows down internal mass transport. Despite the slower PMS transport, the larger cavity provides a greater internal surface area for catalytic reactions, favoring $^1O_2$ accumulation, as reflected by the higher simulated $^1O_2$ concentration (Figs. 4g-i). Based on the short-time approximation of the Fickian diffusion model, PMS transport in HMCS$_{0.2}$ and HMCS$_{0.5}$was assessed from the linear correlation between Qt/Q∞ and t$^{1/2}$. The apparent diffusion parameter ($D\ /r_0^2$) increased from 3.46×10^{-4} s^{-1} for HMCS$_{0.5}$ to 5.73×10^{-4} s^{-1} for HMCS$_{0.2}$, indicating an approximately 1.66-fold improvement in apparent PMS transport (Text S6 and Figure S23). These results suggest that mesoporous channels primarily promote oxidant transport, whereas the hollow cavity provides a relatively stable microenvironment for catalytic reactions.

Overall, the hollow mesoporous architecture establishes a cooperative transport–reaction framework. The mesoporous channels act as accelerated pathways for oxidant delivery, promoting rapid PMS transport and local enrichment near the catalytic interfaces (Meng et al., 2024). Meanwhile, the hollow cavity provides a relatively stable microenvironment that enables sustained catalytic reactions and facilitates the accumulation of reactive intermediates (Diao et al., 2025). The cavity size therefore plays a key role in regulating the balance between mass transport efficiency and reactive surface availability. Smaller cavities favor faster oxidant transport and higher local PMS concentration, whereas larger cavities may expose more accessible inner interfacial space (Han et al., 2022) that promotes the generation of $^1O_2$. This mesoscale coupling between transport and reaction provides a mechanistic explanation for how cavity geometry modulates catalytic performance beyond conventional surface active-site effects.

3.5. Degradation pathway of DCF

Density functional theory calculations revealed that the highest

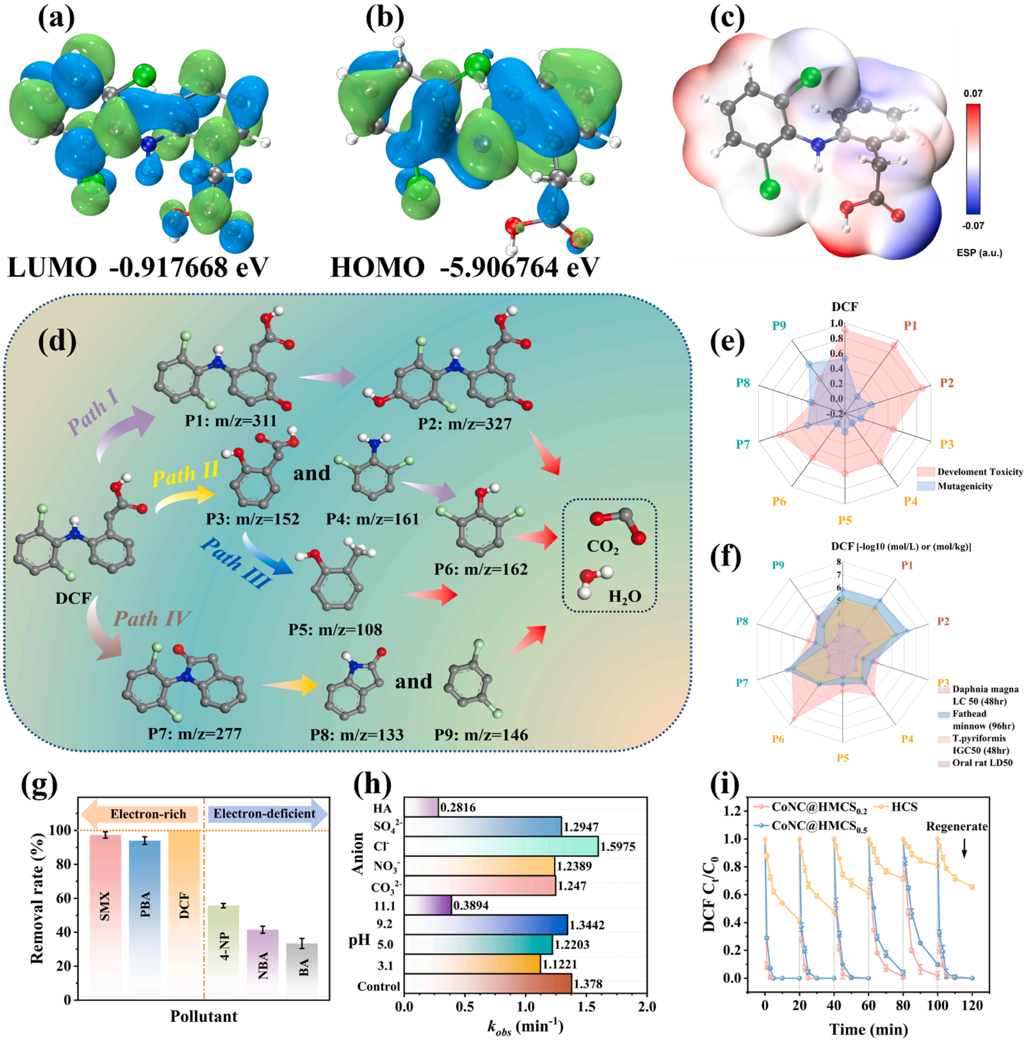

Fig. 5. The distributions of HOMO (a), LUMO (b) and ESP (c) for DCF molecule; the proposed degradation pathways of DCF (d); Toxicity evaluations of DCF and the intermediates, involving developmental toxicity (e), mutagenicity (e), Daphnia magna LC50 (48hr) (f), Fathead minnow (96hr) (f), T.pyriformis IGC50 (48hr) (f), Oral rat LD50 (f); removal rate of different organic pollutants including SMX, PBA, DCF, 4-NP, NBA, and BA (g); DCF degradation kinetics under different initial pHs and with environmentally relevant ions (h); DCF removal efficiencies during cyclic operation (i).

occupied molecular orbital (HOMO) and lowest unoccupied molecular orbital (LUMO) energies of DCF are approximately −5.91 eV and −0.92 eV, respectively, with an energy gap of approximately 5.00 eV, reflecting the relatively stable electronic structure of DCF (Uzzaman et al., 2021) (Figs. 5a and 5b). Notably, the HOMO electron density is predominantly localized over the aromatic ring-NH—CO—C (aromatic ring) moiety, endowing this region with strong electron-donating capability and suggesting that this moiety is favorable for electron-transfer oxidation (Liang et al., 2024). Meanwhile, electrostatic potential (ESP) analysis (Fig. 5c) shows that the region surrounding the carboxyl group exhibits the most negative potential, particularly localized on the oxygen atoms, indicating a high electron density (Akbari et al., 2024) and identifying this site as a preferential target for electrophilic species such as $^1O_2$ (Zhu et al., 2025). Collectively, these electronic features suggest that DCF is prone to undergo both ETP oxidation and electrophilic addition reactions in the catalytic system.

Based on these insights and LC-MS results (Figures S24 and S25), the pathway degradation mechanism of DCF could be proposed (Fig. 5d). Pathway I (DCF→P1→P2) represented a stepwise hydroxylation process of DCF by $^\bullet OH$, in which the aromatic skeleton was retained and the corresponding products were detected at relatively low concentrations. This suggested pathway I likely made only a minor contribution to the overall degradation process. Pathway IV (DCF→P7→P8/P9) was predominantly governed by $^1O_2$, which initiates the transformation via electrophilic addition to electron-rich aromatic sites (Wang et al., 2024). This behavior was consistent with the well-known selectivity of $^1O_2$ toward aromatic systems bearing electron-donating groups (-NH-), leading to oxidized intermediates through addition-rearrangement-cleavage processes. In contrast, pathway II (DCF→P3/P4) was primarily driven by an ETP mechanism. The relatively low ionization potential enables DCF to donate electrons to the catalytic system (Boerma et al., 2014), thereby inducing bond cleavage and forming intermediates P3 and P4. These intermediates subsequently undergo decarboxylation (pathway III), yielding smaller molecular products such as P5. Notably, the significantly higher abundance of P3-P6 (by 1–2 orders of magnitude) in the CoNC@HMCS$_{0.2}$/PMS system strongly supports the important contribution, and likely predominance, of the ETP pathway.

From an environmental perspective, different degradation pathways exert distinct influences on the evolution of product toxicity (Figs. 5e and 5f). In the $^1O_2$-dominated pathways (I and IV), early-stage intermediates (P1, P2, and P7) largely retain aromatic structures and may incorporate additional polar functional groups, which can preserve or even increase developmental toxicity. In contrast, the electron-transfer pathway (II) facilitates bond cleavage and structural fragmentation, giving rise to intermediates (P3 and P4) with overall reduced toxicity, although the persistence of chlorinated moieties may still contribute to mutagenic risk. As the reaction proceeds through pathway III and the later stages of pathway IV (P5, P6, P8, and P9), continued bond cleavage and ring-opening convert these intermediates into smaller molecules, accompanied by increased LC50 and T.pyriformis IGC50 values and thus lower overall toxicity. Overall, DCF degradation evolves from addition-dominated pathways with toxicity retention toward bond-cleavage-dominated deep transformation with toxicity reduction, highlighting the important role of electron-transfer-driven degradation in mitigating environmental risk.

3.6. Practical applicability of the CoNC@HMCS$_{0.2}$/PMS system

The CoNC@HMCS$_{0.2}$/PMS system exhibited distinct selectivity toward different organic pollutants (Fig. 5g) (Zhao et al., 2022). Notably, electron-rich compounds (SMX and PBA) were removed much more efficiently than electron-deficient ones (4-NP, BA and NBA). This behavior was attributed to the higher electron density of electron-rich substrates, which facilitated electron donation and enhances their susceptibility to electrophilic attack (Feng et al., 2023). In contrast, electron-deficient compounds exhibited lower reactivity due to limited electron availability. These results indicate that the catalytic system has a pronounced selective oxidation ability toward electron-rich substrates, further suggesting that nonradical pathways (ETP or $^1O_2$ involvement) dominate the reaction mechanism.

The apparent k_{obs} for DCF degradation is affected by pH and coexisting ions (Fig. 5h). The system maintained high activity over a broad pH range (acidic to neutral), indicating good pH tolerance. Slightly enhanced kinetics under weakly acidic to neutral conditions were likely associated with more efficient PMS activation and $^1O_2$ generation (Guo et al., 2024). In contrast, a decrease in reaction rate was observed under alkaline conditions (pH ≈ 11), possibly due to PMS instability or altered reactive species pathways (Wacławek et al., 2022). Among the coexisting ions, CO_3^{2-} inhibited the reaction, likely through quenching or competitive consumption of reactive species, whereas Cl^-, NO_3^-, and SO_4^{2-} showed minimal effects, indicating strong anti-interference capability in complex water environments. Among all coexisting species, humic acid (HA) exerted the most pronounced inhibitory effect on DCF degradation. This strong suppression was mainly attributed to its complex structure with abundant electron-rich functional groups, which enabled HA to act as an efficient scavenger of reactive species (especially $^1O_2$) and a competitive substrate in electron-transfer processes (Aeschbacher et al., 2012). In addition, HA could adsorb onto the catalyst surface, blocking active sites and further hindering the interaction between PMS and the catalyst (Qian et al., 2020). As shown in Figure S26, DCF could be rapidly degraded in all tested water matrices, although the degradation rate in real water samples was lower than that in ultrapure water, indicating that complex water constituents exerted a certain inhibitory effect on the reaction process. Nevertheless, the system still maintained high removal efficiency in lake water, tap water, and Pearl River water, demonstrating good resistance to matrix interference.

Reusability tests revealed that CoNC@HMCS$_{0.2}$ maintained stable DCF removal efficiency over multiple cycles, indicating excellent structural stability and durability (Fig. 5i). To evaluate the stability of the catalyst during the reaction, the concentration of leached Co in the post-reaction solution was measured. The results showed that the Co^{2+} leaching level remained low (0.09 $mg \cdot L^{-1}$), indicating that the Co active sites possessed strong coordination stability within the carbon framework and that the catalyst maintained good structural integrity during the reaction (Figure S27). Moreover, its catalytic activity could be fully recovered after ethanol washing, which effectively removed the intermediates accumulated on the catalyst surface (Guo et al., 2026; Zhang et al., 2023). The sustained catalytic performance further supports the robustness of the nonradical pathways, which were less susceptible to catalyst deactivation or active site loss. The CoNC@HMCS$_{0.2}$ column system exhibited high removal efficiencies for both DCF and Rh B under continuous-flow conditions (Figure S28). At the initial stage, the removal efficiencies of both pollutants were close to 100%. Although the removal efficiencies gradually decreased with time, they remained relatively stable overall. After 24 h of continuous operation, the removal efficiencies of DCF and Rh B were still maintained at approximately 78% and 85%, respectively, indicating good operational stability of the system under continuous-flow conditions. Overall, the CoNC@HMCS$_{0.2}$/PMS system demonstrates high selectivity toward electron-rich pollutants, along with strong adaptability and stability, highlighting its potential for practical water treatment applications.

4. Conclusions

In this study, two nanoconfined Co-SACs (CoNC@HMCS$_x$) were constructed to achieve efficient activation of PMS and rapid degradation of organic pollutants. Compared with the unconfined counterpart, CoNC@HMCS$_{0.2}$/PMS exhibited not only a significantly enhanced degradation rate but also a markedly higher PUE of 84.6%, highlighting the critical role of nanoconfinement in promoting oxidant utilization. Mechanistic investigations revealed that the CoNC@HMCS$_x$/PMS system was dominated by nonradical pathways, with $^1O_2$ and ETP synergistically driving pollutant oxidation. Specifically, the $^1O_2$-mediated addition pathway tended to generate oxidation intermediates that retained aromatic structures and therefore showed limited toxicity reduction. In contrast, the ETP pathway facilitated bond cleavage and molecular fragmentation, yielding smaller products with substantially reduced toxicity and thereby contributing more effectively to ecological risk mitigation. The combined theoretical and numerical analyses further elucidated the role of nanoconfinement. DFT calculations suggested that the confined structure enhances PMS adsorption and promotes interfacial charge transfer, thereby facilitating the formation of PMS* and strengthening the nonradical oxidation process. Meanwhile, COMSOL simulations demonstrated that mesoporous channels enhanced mass transfer and local enrichment of oxidants, while the hollow cavity provided a relatively stable microenvironment. The cavity size played a crucial role in regulating fluid dynamics and reaction efficiency, with smaller cavities favoring faster mass transfer and higher oxidant utilization. In addition, the system exhibited pronounced selectivity toward electron-rich pollutants, maintained high activity over a wide pH range, and showed strong resistance to interference from most inorganic ions. Excellent structural stability and reusability were also confirmed through cyclic experiments.

Overall, this study provides a scale-consistent understanding of the role of cavity structures in catalysis, distinguishing it from conventional interpretations based on highly curved models. It highlights that mass-transfer regulation and microenvironment effects, rather than curvature itself, are more closely associated with catalytic enhancement. These findings offer new insights into the design of nanoconfined catalysts for efficient PMS utilization and selective oxidation processes.

CRediT authorship contribution statement

Hao Luo: Writing – review & editing, Writing – original draft, Conceptualization. **Junli Zheng:** Funding acquisition. **Jiaxin Liu:** Data curation. **Junjun Ma:** Supervision. **Rui He:** Resources. **Chuqi Huang:** Software. **Rong Xie:** Visualization. **Qintie Lin:** Funding acquisition, Data curation.

Declaration of competing interest

The authors declare that they have no known competing financial interests or personal relationships that could have appeared to influence the work reported in this paper.

Acknowledgments

This work was supported by the National Natural Science Foundation of China (Nos. 42277240, 42507292), and Guangdong Basic and Applied Basic Research Foundation (No. 2024A1515110079). The authors thank Shenzhen HUASUAN Technology Co.,Ltd. for assistance on theoretical calculations.

Supplementary materials

Supplementary material associated with this article can be found, in the online version, at doi:10.1016/j.watres.2026.126136.

Data availability

The data that has been used is confidential.

References

Aeschbacher, M., Graf, C., Schwarzenbach, R.P., Sander, M., 2012. Antioxidant properties of humic substances. Env. Sci. Technol 46 (9), 4916–4925. https://doi.org/10.1021/es300039h.

Akbari, Z., Stagno, C., Iraci, N., Efferth, T., Omer, E.A., Piperno, A., Montazerozohori, M., Feizi-Dehnayebi, M., Micale, N., 2024. Biological evaluation, DFT, MEP, HOMO-LUMO analysis and ensemble docking studies of Zn(II) complexes of bidentate and tetradentate Schiff base ligands as antileukemia agents. J. Mol. Struct. 1301, 137400. https://doi.org/10.1016/j.molstruc.2023.137400.

Boerma, J.S., Vermeulen, N.P., Commandeur, J.N., 2014. One-electron oxidation of diclofenac by human cytochrome P450s as a potential bioactivation mechanism for formation of 2′-(glutathion-S-yl)-deschloro-diclofenac. Chem. Biol. Interact 207, 32–40. https://doi.org/10.1016/j.cbi.2013.11.001.

Cai, L., Yao, Q., Du, X., Tao, X., Zou, M., Zhou, J., Dang, Z., Lu, G., 2024. Identification of superoxide contribution through the quenching method and model system. ACS ES&T Eng. 4 (9), 2145–2154. https://doi.org/10.1021/acsestengg.4c00187.

Dai, H., Li, N., Ye, J., Zhao, J., He, X., Duan, X., Yan, B., Chen, G., Wang, S., 2023. Confinement boosted heterogeneous advanced oxidation processes. Chem. Eng. J. 472, 144861. https://doi.org/10.1016/j.cej.2023.144861.

Diao, X., Zhang, C., Zhang, Z., Shi, Y., Niu, X., Zhang, S., Li, H., Ji, N., 2025. Curvature-engineered hollow MoS_2 nanoreactors boosted hydrodeoxygenation of lignin derivatives to arenes. Chem. Eng. J. 519, 165327. https://doi.org/10.1016/j.cej.2025.165327.

Fang, Z., Xia, Y., Zhang, L., Liu, J., Li, J., Hu, B., Li, K., Lu, Q., Wang, L., 2024. Building the confined CoS_2/MoS_2 nanoreactor via interface electronic reconfiguration to synchronously enhance activity and stability of heterogeneous Fenton-like reactions. Appl. Catal. B: Environ. Energy 346, 123769. https://doi.org/10.1016/j.apcatb.2024.123769.

Feng, Z., Chen, M., Yang, Q., Wang, Z., Li, L., Zhao, H., Zhao, G., 2023. New insights into selective singlet oxygen production via the typical electroactivation of oxygen for water decontamination. Env. Sci. Technol 57 (44), 17123–17131. https://doi.org/10.1021/acs.est.3c06336.

Fu, W., Liu, Z., Li, D., 2025. Pan, B. Chemistry for water treatment under nanoconfinement. Water. Res. 275, 123173. https://doi.org/10.1016/j.watres.2025.123173.

Gao, Y., Chen, Z., Zhu, Y., Li, T., Hu, C., 2020. New insights into the generation of singlet oxygen in the metal-free peroxymonosulfate activation process: important role of electron-deficient carbon atoms. Env. Sci. Technol. 54 (2), 1232–1241. https://doi.org/10.1021/acs.est.9b05856.

Guo, J., Wang, Y., Shang, Y., Yin, K., Li, Q., Gao, B., Li, Y., Duan, X., Xu, X., 2024a. Fenton-like activity and pathway modulation via single-atom sites and pollutants comediates the electron transfer process. Proc. Natl. Acad. Sci. 121 (3), e2313387121. https://doi.org/10.1073/pnas.2313387121.

Guo, R., Bi, Z., Xi, B., Guo, C., Zhang, H., Lv, N., Hu, G., Xu, J., 2024b. A new generation pathway of singlet oxygen in heterogeneous single-atom Mn catalyst/peroxymonosulfate system. Chem. Eng. J. 481, 148629. https://doi.org/10.1016/j.cej.2024.148629.

Guo, J., Li, Y., Ma, J., Xu, X., 2026. Heterogeneous AOPs from mineralization rate to organic carbon transfer process: OCTP systems and emerging regeneration indicators. Environ. Chem. Saf. 2, 9600014. https://doi.org/10.26599/ECS.2026.9600014.

Han, X., Zhang, T., Wang, X., Zhang, Z., Li, Y., Qin, Y., Wang, B., Han, A., Liu, J., 2022. Hollow mesoporous atomically dispersed metal-nitrogen-carbon catalysts with enhanced diffusion for catalysis involving larger molecules. Nat. Commun. 13 (1), 2900. https://doi.org/10.1038/s41467-022-30520-3.

Li, Z., Li, B., Yu, C., Wang, H., Li, Q., 2023. Recent progress of hollow carbon nanocages: general design fundamentals and diversified electrochemical applications. Adv. Sci. 10 (7), e2206605. https://doi.org/10.1002/advs.202206605.

Li, J., Wang, Y., Wang, Z., Ding, D., 2025. Triggering nanoconfinement effect in advanced oxidation processes (AOPs) for boosted degradation of organic contaminants: a review. Chem. Eng. J. 503, 158428. https://doi.org/10.1016/j.cej.2024.158428.

Liang, J., Zhen, P., Gan, P., Li, Y., Tong, M., Liu, W., 2024. DFT calculation of nonperiodic small molecular systems to predict the reaction mechanism of advanced oxidation processes: challenges and perspectives. ACS ES&T Eng. 4 (1), 4–18. https://doi.org/10.1021/acsestengg.3c00204.

Liang, L., Cao, P., Bai, H., Du, X., Chen, S., Yu, H., Liu, Y., Su, Y., Quan, X., 2025. Role of curvature in modulating electronic structure of active sites on hollow carbon spheres for efficient decontamination in catalytic ozonation process. Appl. Catal. B: Environ. Energy 366, 125067. https://doi.org/10.1016/j.apcatb.2025.125067.

Liu, C., Cao, Y., Cheng, Y., Wang, D., Xu, T., Su, L., Zhang, X., Dong, H., 2020. An open source and reduce expenditure ROS generation strategy for chemodynamic/photodynamic synergistic therapy. Nat. Commun. 11 (1), 1735. https://doi.org/10.1038/s41467-020-15591-4.

Liu, Q., Luo, J., Tang, J., Chen, Z., Chen, Z., Lin, Q., 2022. Remediation of cadmium and lead contaminated soils using Fe-OM based materials. Chemosphere 307, 135853. https://doi.org/10.1016/j.chemosphere.2022.135853.

Liu, T., Xiao, S., Li, N., Chen, J., Zhou, X., Qian, Y., Huang, C.-H., Zhang, Y., 2023. Water decontamination via nonradical process by nanoconfined Fenton-like catalysts. Nat. Commun. 14 (1), 2881. https://doi.org/10.1038/s41467-023-38677-1.

Mao, Y., Ma, W., Zuo, W., Sun, H., Tian, Y., Zhang, J., Li, L., 2026. Breaking planar confinement: tailoring the curvature of nanoconfined catalysts to activate PMS for efficient $^1O_2$ generation. Appl. Catal. B: Environ. Energy 385, 126266. https://doi.org/10.1016/j.apcatb.2025.126266.

Meng, Y., Liu, Y.-Q., Wang, C., Si, Y., Wang, Y.-J., Xia, W.-Q., Liu, T., Cao, X., Guo, Z.-Y., Chen, J.-J., et al., 2024. Nanoconfinement steers nonradical pathway transition in single atom fenton-like catalysis for improving oxidant utilization. Nat. Commun. 15 (1), 5314. https://doi.org/10.1038/s41467-024-49605-2.

Mi, X., Wang, P., Xu, S., Su, L., Zhong, H., Wang, H., Li, Y., Zhan, S., 2021. Almost 100 % peroxymonosulfate conversion to singlet oxygen on single-atom CoN2+2 sites. Angew. Chem. Int. Ed. 60 (9), 4588–4593. https://doi.org/10.1002/anie.202014472.

Miao, J., Zhu, Y., Lang, J., Zhang, J., Cheng, S., Zhou, B., Zhang, L., Alvarez, P.J.J., Long, M., 2021. Spin-State-dependent peroxymonosulfate activation of single-atom M-N moieties via a radical-free pathway. ACS. Catal. 11 (15), 9569–9577. https://doi.org/10.1021/acscatal.1c02031.

Nørskov, J.K., Abild-Pedersen, F., Studt, F., Bligaard, T., 2011. Density functional theory in surface chemistry and catalysis. Proc. Natl. Acad. Sci. 108 (3), 937–943. https://doi.org/10.1073/pnas.1006652108.

Qian, J., Gao, X., Pan, B., 2020. Nanoconfinement-mediated water treatment: from fundamental to application. Env. Sci. Technol 54 (14), 8509–8526. https://doi.org/10.1021/acs.est.0c01065.

Ren, W., Nie, G., Zhou, P., Zhang, H., Duan, X., Wang, S., 2020. The intrinsic nature of persulfate activation and N-doping in carbocatalysis. Env. Sci. Technol. 54 (10), 6438–6447. https://doi.org/10.1021/acs.est.0c01161.

Sing, K.S.W., 1989. The use of gas adsorption for the characterization of porous solids. Colloids Surf. 38 (1), 113–124. https://doi.org/10.1016/0166-6622(89)80148-9.

Tang, M., Wan, J., Wang, Y., Ye, G., Yan, Z., Ma, Y., Sun, J., 2024. Overlooked role of void-nanoconfined effect in emerging pollutant degradation: modulating the electronic structure of active sites to accelerate catalytic oxidation. Water. Res. 249, 120950. https://doi.org/10.1016/j.watres.2023.120950.

Terra, J.C.S., Martins, A.R., Moura, F.C.C., Weber, C.C., Moores, A., 2022. Making more with less: confinement effects for more sustainable chemical transformations. Green Chem. 24 (4), 1404–1438. https://doi.org/10.1039/D1GC03283F.

Tian, Q., Zeng, X.-K., Zhao, C., Jing, L.-Y., Zhang, X.-W., Liu, J., 2023. Exceptional photocatalytic hydrogen peroxide production from sandwich-structured graphene interlayered phenolic resins nanosheets with mesoporous channels. Adv. Funct. Mater. 33 (21), 2213173. https://doi.org/10.1002/adfm.202213173.

Tian, Q., Jing, L., Du, H., Yin, Y., Cheng, X., Xu, J., Chen, J., Liu, Z., Wan, J., Liu, J., et al., 2024. Mesoporous carbon spheres with programmable interiors as efficient nanoreactors for H_2O_2 electrosynthesis. Nat. Commun. 15 (1), 983. https://doi.org/10.1038/s41467-024-45243-w.

Tian, Q., Wang, W., Jing, L., Ye, X., Kong, Y., Huang, X., Li, A., Zheng, Z., Zhang, X., Hu, Q., et al., 2025a. Metalloenzyme-inspired cluster fabrication within mesoporous channels featuring optimized catalytic microenvironments for efficient neutral pH H_2O_2 electrosynthesis. Adv. Mater. 37 (17), 2503169. https://doi.org/10.1002/adma.202503169.

Tian, X., Tosello Gardini, A., Raucci, U., Xiao, H., Zhuo, Y., Parrinello, M., 2025b. Electrochemical potential-driven water dynamics control CO_2 electroreduction at the Ag/H_2O interface. Nat. Commun. 16 (1), 10636. https://doi.org/10.1038/s41467-025-65630-1.

Uzzaman, M., Hasan, M.K., Mahmud, S., Fatema, K., Matin, M.M., 2021. Structure-based design of new diclofenac: physicochemical, spectral, molecular docking, dynamics simulation and ADMET studies. Inform. Med. Unlocked 25, 100677. https://doi.org/10.1016/j.imu.2021.100677.

Wacławek, S., Lutze, H.V., Sharma, V.K., Xiao, R., Dionysiou, D.D., 2022. Revisit the alkaline activation of peroxydisulfate and peroxymonosulfate. Curr. Opin. Chem. Eng. 37, 100854. https://doi.org/10.1016/j.coche.2022.100854.

Wang, J., Wang, S., 2020. Reactive species in advanced oxidation processes: formation, identification and reaction mechanism. Chem. Eng. J. 401, 126158. https://doi.org/10.1016/j.cej.2020.126158.

Wang, L., Xu, H., Jiang, N., Pang, S., Jiang, J., Zhang, T., 2021. Effective activation of peroxymonosulfate with natural manganese-containing minerals through a nonradical pathway and the application for the removal of bisphenols. J. Hazard. Mater. 417, 126152. https://doi.org/10.1016/j.jhazmat.2021.126152.

Wang, M., Tang, Y., Wang, J., Xu, Z., Dong, Q., Ma, T., Lai, B., 2023. Promoted peroxydisulfate activation by nitrogen-doped carbon embedding iron on a nickel foam cathode: performance, mechanism and relationship between CO and $^1O_2$ generation. Chem. Eng. J. 460, 141638. https://doi.org/10.1016/j.cej.2023.141638.

Wang, Y., Lin, Y., He, S., Wu, S., Yang, C., 2024. Singlet oxygen: properties, generation, detection, and environmental applications. J. Hazard. Mater 461, 132538. https://doi.org/10.1016/j.jhazmat.2023.132538.

Wang, N., Yang, J., Li, S., Ren, Z., Xu, Q., 2025. Microenvironment modulation of single-atom sites and its applications in Fenton-like reactions. Chem. Sci. 16 (41), 19072–19098. https://doi.org/10.1039/D5SC05230K.

Wei, Y., Miao, J., Ge, J., Lang, J., Yu, C., Zhang, L., Alvarez, P.J.J., Long, M., 2022. Ultrahigh peroxymonosulfate utilization efficiency over CuO nanosheets via heterogeneous Cu(III) formation and preferential electron transfer during degradation of phenols. Env. Sci. Technol. 56 (12), 8984–8992. https://doi.org/10.1021/acs.est.2c01968.

Wen, J., Dini, D., Hu, H.B., Smith, E.R., 2021. Molecular droplets vs bubbles: effect of curvature on surface tension and Tolman length. Phys. of Fluids 33 (7). https://doi.org/10.1063/5.0057401.

Wu, L., Lin, Q., Fu, H., Luo, H., Zhong, Q., Li, J., Chen, Y., 2022. Role of sulfide-modified nanoscale zero-valent iron on carbon nanotubes in nonradical activation of peroxydisulfate. J. Hazard. Mater 422, 126949. https://doi.org/10.1016/j.jhazmat.2021.126949.

Xiao, Z.-J., Zhou, B.-Q., Feng, X.-C., Shi, H.-T., Zhu, Y.-N., Wang, C.-P., Van der Bruggen, B., Ren, N.-Q., 2023. Anchored Co-oxo generated by cobalt single atoms outperformed aqueous species from the counterparts in peroxymonosulfate treatment. Appl. Catal. B: Environ. 328, 122483. https://doi.org/10.1016/j.apcatb.2023.122483.

Xu, Z., Zhang, Y., Wang, F., Li, Z., Gu, W., Zhang, Y., Xie, H., 2023a. Co single-atom confined in N-doped hollow carbon sphere with superb stability for rapid degradation of organic pollutants. Chem. Eng. J. 452, 139229. https://doi.org/10.1016/j.cej.2022.139229.

Xu, K., Lin, Q., Fan, X., Zheng, J., Liu, Y., Ma, Y., He, J., 2023b. Enhanced degradation of sulfamethoxazole by activation of peroxodisulfate with red mud modified biochar: synergistic effect between adsorption and nonradical activation. Chem. Eng. J. 460, 141578. https://doi.org/10.1016/j.cej.2023.141578.

Yi, H., Almatrafi, E., Ma, D., Huo, X., Qin, L., Li, L., Zhou, X., Zhou, C., Zeng, G., Lai, C., 2023. Spatial confinement: a green pathway to promote the oxidation processes for organic pollutants removal from water. Water. Res. 233, 119719. https://doi.org/10.1016/j.watres.2023.119719.

Yin, K., Wu, R., Shang, Y., Chen, D., Wu, Z., Wang, X., Gao, B., Xu, X., 2023. Microenvironment modulation of cobalt single-atom catalysts for boosting both radical oxidation and electron-transfer process in Fenton-like system. Appl. Catal. B: Environ. 329, 122558. https://doi.org/10.1016/j.apcatb.2023.122558.

You, T., Sun, H., Hua, W., Geng, S., Hu, Z., Shang, Y., Huang, Q., Dai, S., Chen, K., 2025. Insights into Co-catalytic single-atom-support interactions for boosting sulfur reduction electrocatalysis. Angew. Chem. Int. Ed. 64 (16), e202425144. https://doi.org/10.1002/anie.202425144.

Zhang, D., Li, Y., Wang, P., Qu, J., Li, Y., Zhan, S., 2023a. Dynamic active-site induced by host-guest interactions boost the Fenton-like reaction for organic wastewater treatment. Nat. Commun. 14 (1), 3538. https://doi.org/10.1038/s41467-023-39228-4.

Zhang, Y.-J., Chen, J.-J., Huang, G.-X., Li, W.-W., Yu, H.-Q., Elimelech, M., 2023b. Distinguishing homogeneous advanced oxidation processes in bulk water from heterogeneous surface reactions in organic oxidation. Proc. Natl. Acad. Sci. 120 (20), e2302407120. https://doi.org/10.1073/pnas.2302407120.

Zhao, X., Zhang, Z., 2025. Heterogeneous peroxymonosulfate-based advanced oxidation mechanisms: new wine in old bottles? Env. Sci. Technol. 59 (12), 5913–5924. https://doi.org/10.1021/acs.est.4c11311.

Zhao, Y., Zhang, J., Guo, X., Fan, H., Wu, W., Liu, H., Wang, G., 2017. Fe_3C@nitrogen doped CNT arrays aligned on nitrogen functionalized carbon nanofibers as highly efficient catalysts for the oxygen evolution reaction. J. Mater. Chem. A 5 (37), 19672–19679. https://doi.org/10.1039/C7TA05936A.

Zhao, Y., Yu, L., Song, C., Chen, Z., Meng, F., Song, M., 2022. Selective degradation of electron-rich organic pollutants induced by CuO@biochar: the key role of outer-sphere interaction and singlet oxygen. Env. Sci. Technol 56 (15), 10710–10720. https://doi.org/10.1021/acs.est.2c01759.

Zhao, X., Khan, I.A., Asif, M.B., Zhang, Z., 2026. Nanoconfinement-based catalysis for advanced water treatment. Appl. Catal. B: Environ. Energy 381, 125877. https://doi.org/10.1016/j.apcatb.2025.125877.

Zhou, X., Zhao, Q., Wang, J., Chen, Z., Chen, Z., 2021. Nonradical oxidation processes in PMS-based heterogeneous catalytic system: generation, identification, oxidation characteristics, challenges response and application prospects. Chem. Eng. J. 410, 128312. https://doi.org/10.1016/j.cej.2020.128312.

Zhu, Z.-S., Wang, Y., Wang, P., Zhong, S., Hu, K., Ren, S., Vongsvivut, J.P., Sun, H., Duan, X., Wang, S., 2025a. Multidimensional engineering of single-atom cobalt catalysts for ultrafast Fenton-like reactions. Nat. Water 3 (2), 211–221. https://doi.org/10.1038/s44221-024-00382-8.

Zhu, T., Qi, F., Tao, C., Li, Y., Li, S., Lv, X., 2025b. Predicting reaction rate constant of organic compounds with singlet oxygen and revealing its contributors using machine learning. Ind. Eng. Chem. Res. 64 (8), 4282–4292. https://doi.org/10.1021/acs.iecr.4c04008.

Zou, Y., Hu, J., Li, B., Lin, L., Li, Y., Liu, F., Li, X.-y., 2022. Tailoring the coordination environment of cobalt in a single-atom catalyst through phosphorus doping for enhanced activation of peroxymonosulfate and thus efficient degradation of sulfadiazine. Appl. Catal. B: Environ. 312, 121408. https://doi.org/10.1016/j.apcatb.2022.121408.

Zuo, S., Ding, Y., Cheng, H., Guan, Z., Li, X., Li, D., 2024. Confinement effect of FeMOFs glass enhances the proton coupled electron transfer reaction for the organic pollutants polymerization toward sustainable water purification. Chem. Eng. J. 491, 152170. https://doi.org/10.1016/j.cej.2024.152170.